JASA ARTICLE

Random *versus* regular square lattice experimental comparison for a subwavelength resonant metasurface

Martin Lott[a] and Philippe Roux
University Grenoble Alpes, University Savoie Mont Blanc, CNRS, IRD, IFSTTAR, ISTerre, 38000 Grenoble, France

ABSTRACT:
An experimental comparison is reported here between two equivalent resonant subwavelength metasurfaces made of long aluminum beams glued closely together on a thin aluminum plate. One metasurface has a random distribution of the resonator beams, and the other has a regular square lattice of pitch 1.5 cm. The random lattice shows the "resonant" behavior of a typical metasurface, with a wide full bandgap for the first A_0 Lamb mode. Instead, the regular square lattice combines Fano resonance with Bragg scattering at the edges of the passband, thus creating anisotropy and a pseudo bandgap. Comparisons with numerical simulations are performed, with good agreement with the experimental data. The multimodal response of the beams is also responsible for double negativity in a narrow frequency band, and the event of a pseudo bandgap around this same flexural resonance. In addition, the scattering regimes for both the random and regular metasurfaces are characterized using coherent and incoherent signal analysis. © *2021 Acoustical Society of America*. https://doi.org/10.1121/10.0005060

(Received 31 December 2020; revised 24 March 2021; accepted 3 May 2021; published online 27 May 2021)
[Editor: Olga Umnova] Pages: 3645–3653

I. INTRODUCTION

Metamaterials are artificially structured media that show extreme mesoscopic properties for waves that travel through them. Since the early 2000s, metamaterials have emerged widely throughout the numerous areas of physics where electromagnetic, elastic, and acoustic waves are studied. They can provide the possibility to control the wave flow in an unprecedented way, with important consequences in material sciences and engineering.

In terms of the ease of handling centimetric waves in the laboratory (Yves *et al.*, 2018; Yves *et al.*, 2020; Lott *et al.*, 2019b), metamaterials have other aspects of interest in experimental physics. These can reproduce the complexities of wave–matter interactions at a human scale, which usually requires heavily controlled experimental set-ups (Juffmann *et al.*, 2013). Here, the strategy is somehow different: artificial objects can be engineered that are organized on a scale smaller than the operating wavelength, and that interact with waves to induce new "mesoscopic" observations.

Among the different classes of metamaterials, there are those in the which their physics is driven by periodic structures that induce Bragg scattering, also known as crystal phononics in acoustics, and crystal photonics in optics. These can be distinguished from those where their physics is controlled by the local resonance of their unit cell, which induces hybridization phenomena. To summarize, typical phononic/photonic crystals are spatially ordered at the wavelength scale, when locally resonant metamaterials can be spatially disordered, as long as there are enough resonators within one wavelength; i.e., they are structured at the subwavelength scale.

Two-dimensional (2D) periodic structures, or locally resonant (metasurface) equivalent systems, have revolutionized the control of waves in recent years (Lauterbur, 1973; Engheta and Ziolkowski, 2006; Cai and Shalaev, 2010). The main physical properties of these structured media can be directly derived from the complex dispersion relation $k(w)$ (Smith *et al.*, 2004; Krushynska *et al.*, 2017; Lott *et al.*, 2019a). Such properties include, for example, opening of band gaps (Capolino, 2017; Colombi *et al.*, 2014), slow-wave frequency bands (Pendry *et al.*, 2006; Pendry, 2000; Leonhardt, 2006; Pomot *et al.*, 2020; Page, 2016), and spatial filtering (Veselago, 1967; Capolino, 2017), among others. This rich but sometimes hard to interpret information is of crucial relevance for the design of metamaterial-based devices. The real part of the wavenumber $k(w)$ is associated with the propagative (dispersive) properties and drives the spatial resolution characteristics of the metamaterial, while its imaginary part is related to attenuation.

In practice, 2D crystals based on Bragg interferences have the major drawback of a spatial period that is comparable to the wavelength, which makes subwavelength resolution difficult to achieve. Recent studies have thus tried to combine resonance and the Bragg phenomena with the study of wave responses of subwavelength periodic metasurfaces (2D metamaterials) made of resonant units (Colombi *et al.*, 2017). In particular, as in Bragg type 2D crystals, multiple scattering and strong near-field coupling have profound consequences in locally resonant metasurfaces, despite their subwavelength scale (Yves *et al.*, 2020; Kaina *et al.*, 2013).

[a]Electronic mail: martin.lott@univ-grenoble-alpes.fr, ORCID: 0000-0002-7097-9424.

In contrast to acoustic and electromagnetic systems, elasto-dynamic media such as metallic plates have the advantage of supporting Lamb waves with different polarization. This allows for mode conversion at the resonator–plate attachment, which induces monopolar and dipolar resonance effects. Among the possible resonant metasurface designs for plate waves proposed in recent years (Baravelli and Ruzzene, 2013; Miniaci *et al.*, 2015; Lee *et al.*, 2018; Matlack *et al.*, 2016, Galich *et al.*, 2017; Tallarico *et al.*, 2017], those that provide resonant metasurfaces with superior characteristics and versatility of use propose a cluster of long metallic beams (i.e., the resonators) attached to a metallic plate (Pennec *et al.*, 2008; Wu *et al.*, 2011; Achaoui *et al.*, 2011; Colombi, 2016).

The first-order physics of this metasurface is well described through a Fano-like resonance (Miroshnichenko *et al.*, 2010; Colquitt *et al.*, 2017). A single beam attached to a plate couples with the out-of-plane motion of the A_0 Lamb mode. This monopolar coupling is particularly strong at the compressional anti-resonance of the beam. As for the metasurface discussed here, when the resonators are arranged as a subwavelength cluster [i.e., with λ (the wavelength of the plate waves) much greater than the resonator spacing], the resonance of each beam acts constructively to enlarge the bandgap, until it approximates the resonance (half wavelength) of the beam [Rupin *et al.*, 2014; Colombi *et al.*, 2017]. Thus, the resulting bandgap is broad, and it appears independent of the random *versus* regular clusters of beams on the metasurface. Note that, when the plate gets thinner, dipolar coupling is also observed at the flexural resonances of the beam, which can lead to localized states due to multi-wave interactions at the beam–plate attachments (Lott *et al.*, 2020).

In this paper, the experimental investigations involve such locally resonant metasurfaces that are made of long vertical beams attached to a thin plate. The complex dispersion relation and the frequency-dependent spatial wavefields are compared for subwavelength clusters of resonators that are random and regular. When approaching the bandgap, it is demonstrated experimentally here that hybridization effects associated with the Fano resonance tend to strongly diminish the effective wavelength of the metasurface. In this way, low-frequency Braag scattering, which induces strong anisotropy effects, can appear with the periodic (regular) arrangement of the beams.

This paper is structured as follows. First, the experimental set-up and methodology are presented, as applied to the recorded spatial–temporal data from which the dispersion relation $k(\omega)$ for both the random and regular metasurfaces is extracted. We discuss then the phase and amplitude wavefield representations at a set of discrete frequencies that illustrate the low-frequency Bragg scattering effects in the regular configuration. The time-dependent scattered intensity is compared at the source location for both the random and regular metasurfaces, which allows our results to be linked to a classical mesoscopic wave physics effect. Finally, we also study the regular metasurface at the flexural resonance of the beams, and we report the first experimental evidence of anisotropy and double negativity behavior around this dipolar resonance.

II. EXPERIMENTAL SET-UP

The study set-up is based on two metasurfaces that are built on two separate thin aluminum plates (length, 2 m; width, 1 m; thickness, 2 mm). The experimental scheme is shown in Fig. 1. The plate has one round boundary shape to break its natural symmetry. One random configuration [Fig. 1(a-1)] and one regular square array [Fig. 1(a-2)] of long aluminum beams (length, 60 cm; diameter, 6 mm) that act as resonators are glued vertically (bicomponent Araldite glue) onto each plate surface. Both of these metasurfaces have the same surface density of $\sim$0.5 beams/cm^2. The frequency bandwidth investigated (1–3 kHz) limits the plate waves to the first symmetric and antisymmetric Lamb modes. Due to the particularly thin plates, most of the energy inside this frequency band propagates in an antisymmetric mode A_0 that is characterized by out-of-plane polarization. At around 2.5 kHz, the A_0 wavelength is 12 cm, with a wave speed of 300 m/s. The S_0 is much faster at the same frequency, with a wavelength of 2 m for a wave speed of 5000 m/s. The first antisymmetric A_0 Lamb wave mode is generated inside the plate using two piezoelectric 12-mm-diameter disks (ABT-456-RT), with a resonant frequency of around 10 kHz outside the frequency band of the study. One of the piezo sources is located at the center of the cluster of beams, and the other is in the far-field of the metasurface area. A 3-s-long electrical chirp signal is applied to the piezo source, with a frequency ramp starting at 1 kHz and going up to 8 kHz. The wavefield is then recorded with a three-component laser vibrometer (PSV-500–3D Xtra; Polytech), and cross-correlated with the emitted signal, to provide a 500-ms highly reverberated impulse response with an 80 dB signal-to-noise ratio for each component [Fig. 1(e)]. The three heads of the laser vibrometer are mounted on a five-axis motorized robot (KR 120 R3500K Prime) that allows full three-dimensional (3D) measurements of the plate + beams wavefield from above [Fig. 1(b)] and below [Fig. 1(c)]. For the two metasurfaces (random and regular), three scanning areas are defined, for which the wavefield is accurately sampled due to the motion of the robot arm. The first zone includes the plate in the metasurface region, on the opposite side of the plate with regard to the cluster of beams. The second zone is a free plate region that is distant from the metasurface area, and the last zone is the top of the beams. The final dataset gathers the exact position in the robot repository and the three-component velocity field at each of the scanned points for each metasurface (random and regular). Due to the expected drop in velocity, the two independent metasurface areas are spatially sampled with a 4-mm step grid, while the free plate surface is scanned with an 8-mm step grid. The resonator motion is measured with one point at the top of the beam. A control unit drives the robot and the laser and generates and records the signals. The noninvasive measurement with a scanning laser is essential

https://doi.org/10.1121/10.0005060

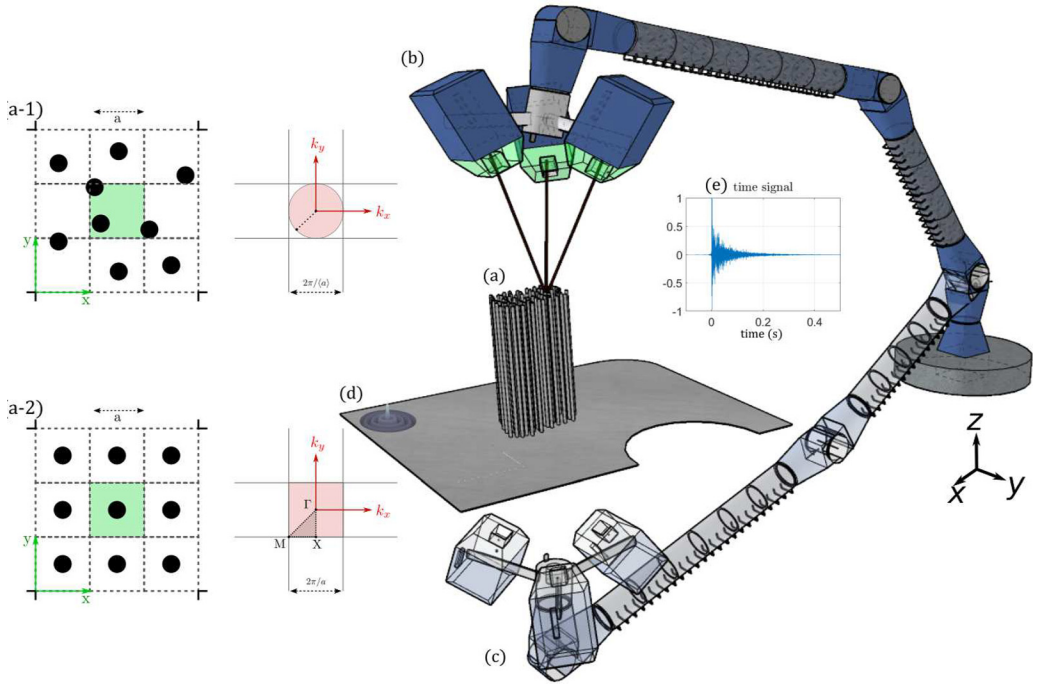

FIG. 1. (Color online) Scheme of the experimental set-up. The metamaterial (a) is constituted of long aluminum beams glued to a thin (2-mm thick) aluminum plate. Two distributions for the beams are considered as, (a-1) a random distribution with an average distance between the beams of $<a> = 1.5$ cm, and (a-2) a regular square lattice of pitch a=1.5 cm that defines the unit cell of the metasurface. A three-component laser head (b) extracts the full wavefield at the top of the beam and at the plate surface (c), resulting from two independent sources, inside and outside (d) the metasurface. (e) A typical recorded signal at the plate surface (out-of-plane motion). The plate is highly reverberating, with 0.5 s of recorded coda.

for optimal wavefield analysis of the plate–beams system. Note, however, that with 10 s acquisition per scanned point and two different sources, the full dataset measurement took approximately 24 h for each of the two metasurfaces.

III. DATA ANALYSIS

For each metasurface, the dispersion curves are computed from the estimation of the cross-spectral density matrix (CSDM) and the correlation of the CSDM with a model-based plane-wavefield with varying wave vector amplitude and direction (Seydoux *et al.*, 2017; Baggeroer *et al.*, 1988). First, at frequency f, the CSDM $K(f)$ is estimated as follows:

$$K_{ij}(f) = \left\langle \tilde{d}(f, \vec{r}_i)\tilde{d}(f, \vec{r}_j)^* \right\rangle, \tag{1}$$

where $\tilde{d}(f, \vec{r}_i) = d(f, \vec{r}_i) / \left| d(f, \vec{r}_i) \right|$ is the normalized Fourier transform (keeping the phase only) of the out-of-plane wavefield component measured from the laser vibrometer in $\vec{r}_i$, for a finite-duration recording window of duration δt, starting at time T. * indicates the Hermitian transpose operation. We take advantage of the equipartition of the spatial wavefield inside the plate to perform a temporal ensemble average [indicated by the <> signs in Eq. (1)] for the CSDM estimation over the two piezo sources and the different time windows T. In practice, we choose a starting time T that expands from 50 ms (for the wave mixing to be sufficient) to 350 ms (where the noise starts to dominate) for both sources, $\delta t = 35$ ms and an ensemble of 512 spatial receiving points $\vec{r}_i$ chosen randomly inside the metasurface area.

Second, we proceed to the artificial isotropization of the wavefield by normalization of the eigenvalues of the CSDM (Seydoux *et al.*, 2017). This method allows the direction of space with the low intensity level to be balanced, which greatly influences the quality of the CSDM estimation. This step requires singular value decomposition of the CSDM at each frequency. From the normalized singular values distribution $[\lambda_1, \ldots, \lambda_n]$, the Shannon entropy (Seydoux *et al.*, 2017; Lott *et al.*, 2020) is computed as

$$S = -\sum \lambda_i \log \lambda_i. \tag{2}$$

This parameter is related to the number of degrees of freedom; i.e., the number of modes that are encoded in the CSDM. The idea here is to balance equally the intensity of each mode in the CSDM estimation. The number of excited modes at each frequency is estimated as the exponential of the entropy,

$$n = \lceil e^S \rceil. \tag{3}$$

Then, the normalized CSDM $\tilde{K}(f)$ is computed from the n first eigenvectors V_p of $K(f)$ as

$$\tilde{K}(f) = \sum_{p=1}^{n} V_p V_p^*. \tag{4}$$

Finally, the dispersion curves are retrieved for both the random and regular metasurfaces by matching the CSDM

matrix $\tilde{K}(f)$ against the plane wave synthetic field $T_0 = e^{i\vec{k}.\vec{r}}$ (with $\vec{k}$ defined as the wave vector, and $\vec{r}$ as the spatial position of the receivers) using a cross correlation operator. The beamforming output is defined for each wave vector amplitude and direction as

$$B(\vec{k}, f) = \left| T_0^*(\vec{k}) \tilde{K}(f) T_0(\vec{k})^+ \right|. \quad (5)$$

For the random arrangement of the beams, as all directions are equivalent, we proceed to an azimuthal averaging and report the results as a function of the wave vector amplitude k only. For the regular configuration of the beams, the beamforming calculation is limited to inside the well-known irreducible Brillouin zone defined on the wave vector plate $k = (kx, ky)$ by the three point coordinates: $\{\Gamma = (0, 0), M = (\pi/a, \pi/a), X = (\pi/a, 0)\}$, where a is the pitch array of the resonators. By browsing through the possible values of $\vec{k}$ along the path $\Gamma - X - M - \Gamma$ [see Fig. (1a-2)], $B(\vec{k},f)$ is computed for the overall considered frequency bandwidth. Finally, $B(\vec{k},f)$ is averaged over all four symmetry directions of the cell.

In addition, the 3D elastic problem is solved numerically, including all of the admissible modes for the discretized plate + beam system. An eigenvalue analysis on a single cell is used with Bloch–Floquet periodic boundary conditions to mimic the infinite array of spatially ordered beams, as in Colombi *et al.* (2017). As for the experimental configuration, the numerical cell is made up of a $1.5 \times 1.5\,\text{cm}^2$ square unit cell of the plate, which is centered on the elongated beam. The beam is 61.5 cm long and 5.8 mm in diameter. The bulk density, Young's modulus, and Poisson's ratio are set to $2700\,\text{kg/m}^3$, 69.10^9 GPa, and 0.33, respectively. The "true" value (6 mm) for the beam diameter in the simulation is modified to include the experimental attachment of the beams onto the plate (i.e., imperfections due to the glue), which decreases the apparent bending stiffness of the beams. The dispersion curves obtained from the simulations are reported superimposed on the experimental curves in Fig. 2, panel 2, according to the norm of the wave number $||\vec{k}||$, along the path $\Gamma - X - M - \Gamma$.

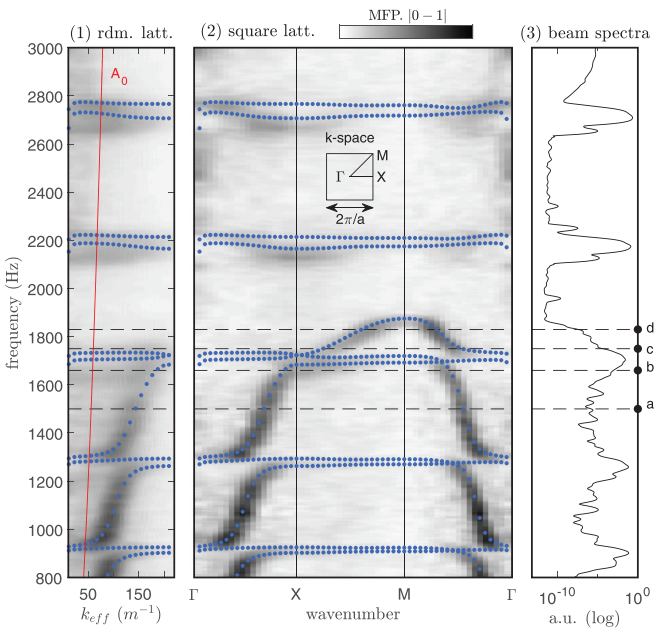

FIG. 2. (Color online) (1, 2) Dispersion curves measured from the experimental data for the random lattice with azimuthal averaging (1), and for the regular lattice on the Brillouin edges $\Gamma - X - M - \Gamma$ (2). (3) Flexural motion spectra, at the top of the beams.

IV. DISPERSION RELATIONS FOR THE RANDOM AND REGULAR METASURFACES

Figure 2 presents the dispersion curves obtained with the random lattice (Fig. 2, panel 1) and the regular square lattice (Fig. 2, panel 2), in gray scale. The beam motion spectra for the square lattice is shown in Fig. 2, panel 3, considering an average of the in-plane directions (x and y) over the set of resonators in the metasurface. Numerical simulation for the Brillouin zone $\Gamma - X - M - \Gamma$ is depicted with blue dots in Fig. 2, panel 2. Also, the free plate response A_0 is depicted in red in Fig. 2, panel 1, along with the numerical simulation for the $\Gamma - X$ direction (blue dots), which assumes that the average inter-beams distance is the same in the ordered and random configurations. The agreement between the numerical simulations and the experimental data is excellent. As previously reported by Rupin *et al.* (2014) and Williams *et al.* (2015), the 2D random metasurface (Fig. 2, panel 1) can be appropriately modeled by a one-dimensional (1D) regular metasurface, with a lattice size equal to the average distance between the resonators, which we validate here.

Between 800 and 1650 Hz, the random and regular metasurfaces show the same kind of behavior. In Fig. 2, panel 2, the directions $\Gamma - X$ and $\Gamma - M$ are equivalent and no anisotropy is discernable on the Brillouin edges. However, the presence of flexural resonance, which is indicated by the isolated picks in Figs. 2, panel 3, a–d, provokes sharp bending of the dispersion curves, which reaches the edges of the Brillouin zone. This means that the metasurface behavior oscillates between supra-wavelength (the wavelength in the metasurface region is larger than in the free plate) and sub-wavelength (the wavelength in the metasurface region is smaller than in the free plate), even in the frequency bandwidth of the first passband. The broad wavelength interval can be read from Fig. 2, panel 1, with an effective wavelength λ that spreads out between $\lambda \sim 12$ cm, (corresponding to ~ 8 unit cells) and $\lambda \sim 3$ cm, (corresponding to ~ 2 unit cells. Through their first compressional resonance, the beams act alternatively (as a function of frequency) as a mass or a spring, which dictates the appearance of passband and bandgap (Lott and Roux, 2019b). The stopband boundaries depend on the minima and maxima of the rod impedance, calculated as a vertical force on the plate, as shown by Williams *et al.* (2015). For the random lattice, this starts at around 1700 Hz; for the regular lattice, a Bragg bandgap in the $\Gamma - X$ direction is observed, and the main bandgap starts only at 1900 Hz, i.e., 200 Hz after the random lattice. The presence of a Bragg bandgap in

https://doi.org/10.1121/10.0005060

such a low-frequency regime is due to the slowing down of the waves, and thus to a strong decrease in the wavelength of the A_0 mode inside the metasurface. Note that, at the passband edges between 1700 and 1900 Hz, the wavelength becomes on the order of a unit cell [Fig. 1(a-2)], and only the diagonal of the unit cell is an admissible propagating direction as will be discussed later in Figs. 4, column 3, c and d. After 1900 Hz, no wave can propagate in the stopband. At around 2200 and 2800 Hz, the flexural motion of the beams induces sharp leakage inside the main bandgap. From the simulation results, two branches are visible around each flexural resonance (Fig. 2, panels 1 and 2, blue dots). This corresponds to degeneration of the bending mode of one beam into two closed quasi-flat branches. However, these branches are not discernable in the experimental data. The time window δ t used in the signal processing analysis and the finite size of the sample prevent the identification of these two flexural modes. In Sec. V, we focus on the passband, and in particular on four frequencies, at 1500, 1690, 1750, and 1830 Hz, as highlighted with black dots in Fig. 2, indicated by the labels a, b, c, and d.

V. WAVEFIELD PATTERNS AT SELECTED FREQUENCIES

In Figs. 3 and 4, other views of the typical wavefield recorded for both of the metasurfaces are shown, putting in parallel the phase (Figs. 3 and 4, column 1), the diffused intensity from the source (Figs. 3 and 4, column 2), and the spatial Fourier representation in a (k_x, k_y) graph (Figs. 3 and 4, column 3). The phase is computed as the argument of the temporal Fourier transform of each recorded signal, with the source inside the metasurface. The intensity is the square of the Fourier modulus at a given frequency (as a log scale), also with the source inside, but at an early stage of the propagation (<10 ms), and the spatial Fourier transform is computed for every (k_x, k_y) possible value, stacking over small temporal windows in the diffuse coda of both sources. The

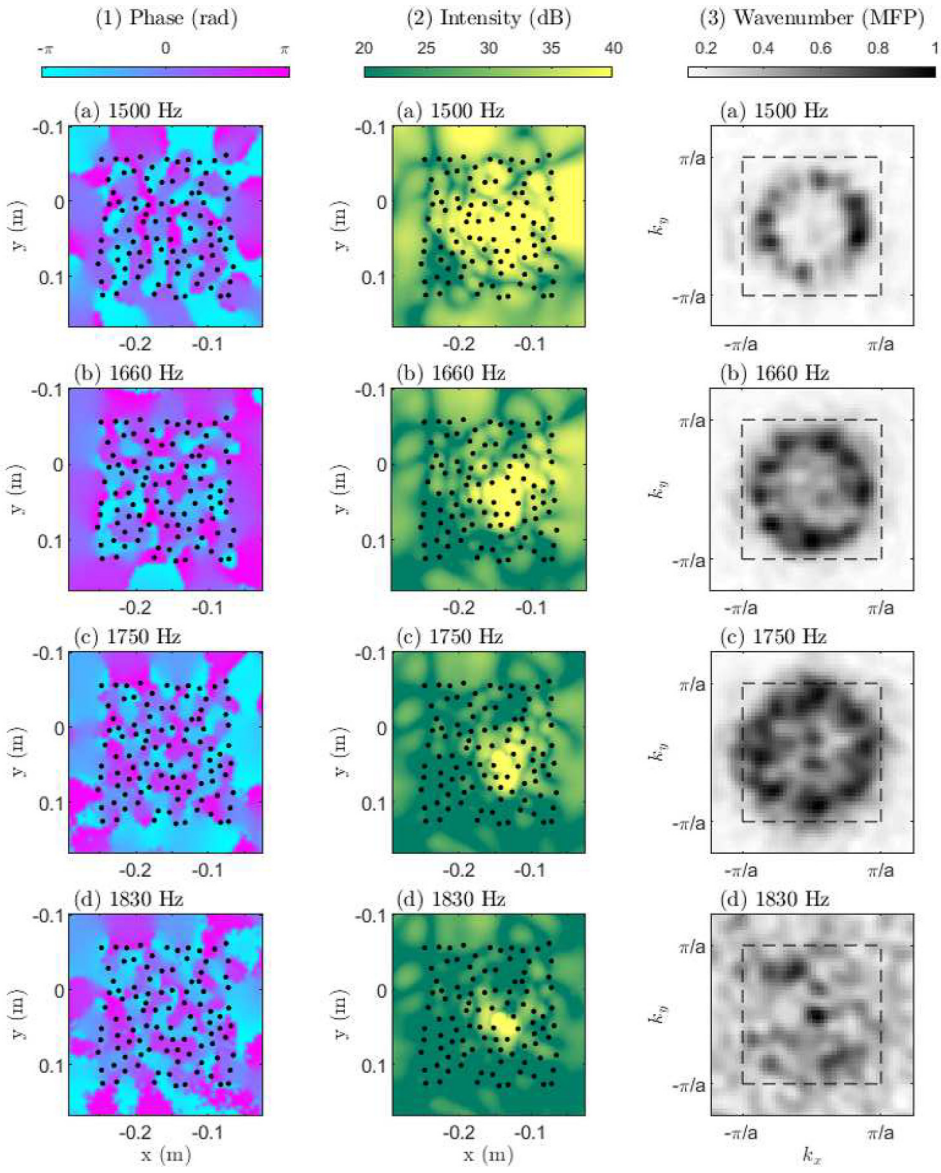

FIG. 3. (Color online) Wavefield patterns measured in the random lattice, for the phase (1, rad), intensity (2, dB), and in the reciprocal space (k_x, k_y; 3), for the four frequencies of 1500 Hz (a), 1690 Hz (b), 1750 Hz (c), and 1830 Hz (d). The theoretical Brillouin limit (not valid here in the random configuration) is also shown for comparison with Fig. 3, as the black square areas in column 3.

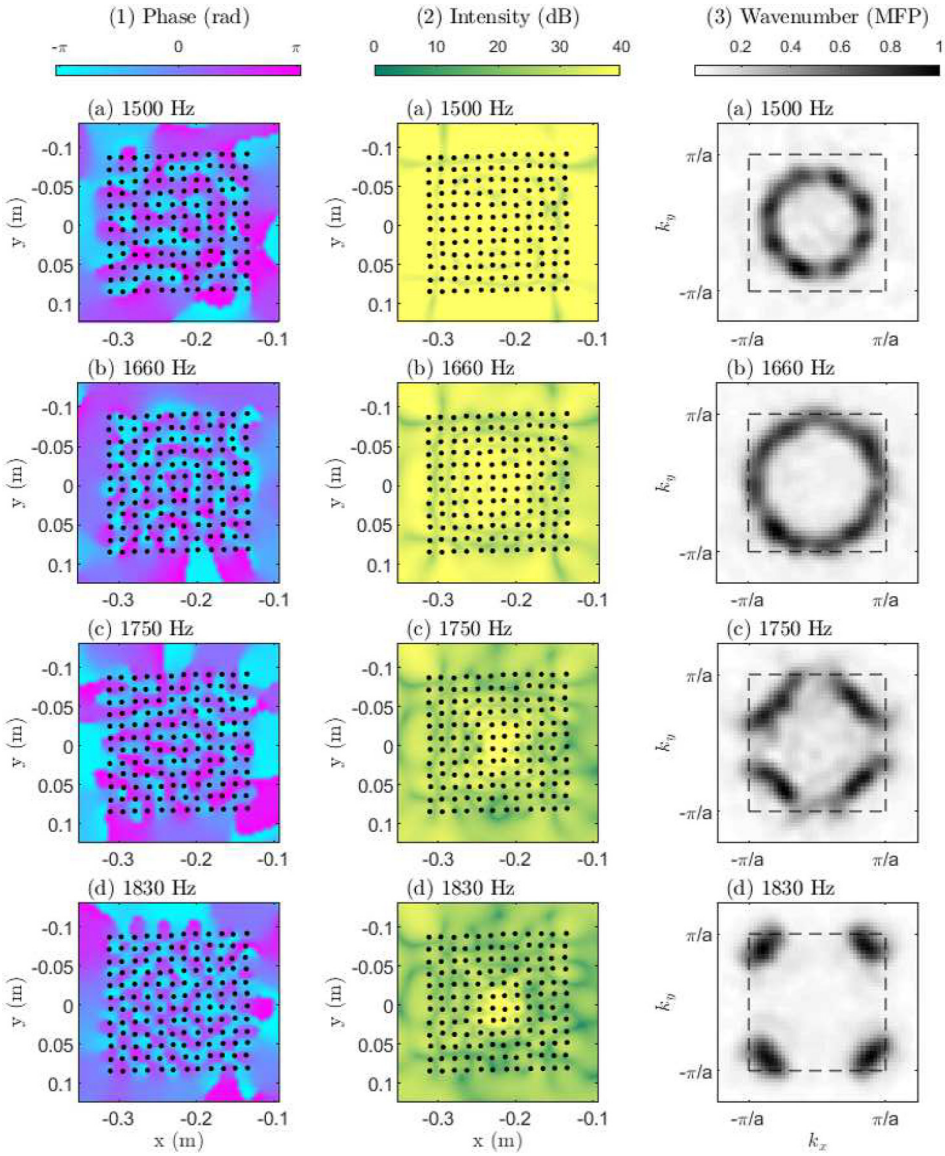

FIG. 4. (Color online) Wavefield patterns measured in the regular lattice, for the phase (1, rad), intensity in (2, dB) and in the reciprocal space (k_x, k_y; 3), for the four frequencies of 1500 Hz (a), 1690 Hz (b), 1750 Hz (c), and 1830 Hz (d). The theoretical Brillouin limit is shown as the black square areas in column 3 for $(k_x, k_y) \in [-(\pi/a)\,(\pi/a)]^2$.

black square areas in Figs. 3 and 4, column 3, show the theoretical Brillouin limit $(k_x, k_y) \in [(\pi/a)(\pi/a)]^2$ that cannot be exceeded in the regular lattice configuration.

For the random lattice, three main observations can be made here; first, the reciprocal space shows "imperfect" (distorted) radiation circles without clear anisotropy (Fig. 3, column 3, a–d), even after 1750 Hz (Fig. 3, column 3, c). The intensity leakage from the source at the early time of the propagation is more heterogeneous here (Fig. 3, column 2, a–d) than for the regular square lattice (Fig. 4, column 2, a–d), as will be discussed in the next paragraph. Second, the phase reveals a diffuse speckle in the passband below 1750 Hz (Fig. 3, column 1, a–d). From previous studies (Lott *et al.*, 2020), we know that the scattering effects in this random lattice can be very intense, which is translated here into the no isotropic spreading of the intensity (Fig. 3, column 2) and into the distortion of the radiated circle in the reciprocal space (Fig. 3, column 3). Finally, the intensity field at and above 1750 Hz, i.e., in the main bandgap of the random lattice, is limited to evanescent waves around the point source (Lott *et al.*, 2019b), as no intensity leakage is allowed from the inside to the outside of the metasurface.

For comparison, in Fig. 4, the same representations show the wavefield inside the regular square lattice at the same frequencies. At around 1500 and 1690 Hz (Fig. 4, horizontal panels, a and b), no anisotropy is seen for the spatial Fourier representation, with a clear circle inside the Brillouin limit (Fig. 4, column 3, a and b). Note that without the procedure described earlier on the normalization of the eigenvalues of the CSDM, the expected circle would have been less obvious (for further explanation, see Seydoux *et al.*, 2017). At both frequencies, the phases of the wavefields (Fig. 4, column 1, a and b) highlight smaller wavelengths inside the metasurface than for the free plate, and the intensity leaks from the inside to the outside of the metasurface.

After 1750 Hz, the energy leakage from the source inside the metasurface is anisotropic (Fig. 4, horizontal panels, c and d). The "cross-shape" anisotropy spreading starts to be visible, as previously reported by Colombi *et al.*

https://doi.org/10.1121/10.0005060

(2017) with numerical simulations. In the present case of a reverberated wavefield, plane waves can be seen to travel only in the diagonal of the beam cluster. For 1830 Hz, Fig. 4, column 1, d, shows the superposition of these two-plane waves, which propagate in a perpendicular direction. In the reciprocal space, two isolated directions can be seen for the propagating waves with nonzero coherence. In the $\Gamma - X$ direction, there is no propagation.

Going back to the random *versus* regular metasurface configurations below 1750 Hz (Figs. 3 and 4, columns 1–3, a and b), no distortion of the radiation circle in the reciprocal space of the ordered metasurface is observed. This is actually as expected, according to the Bloch-Floquet theorem. In a regular lattice, the scattering does not break the flatness of the wave passing through, which differs from a random lattice (Lott and Roux, 2019b). Here, for this specific study of random *versus* regular lattice, we interpret a consequence of this theorem in the following way. The scattering inside the regular square lattice is fully coherent. The interferences of the multiple scattering that occurs at the base of each beam are constructive. In the random lattice, the destructive interferences in the resulting wavefield (Fig. 3) highlight the incoherence of the scattering process.

As we use the same source piezoelectric disks, generator, amplifier, and plate geometry for both metasurfaces, a ratio of two is expected between the intensity measured in the regular square lattice, and the intensity measured in the random lattice. To demonstrate this, two small areas are selected (smaller than the wavelength) around the sources located inside each metasurface, and the average diffuse intensity is computed in the frequency band of 1.5 Hz to 1.7 kHz in this area. Figure 5(a) shows the average intensity envelope for both of the metasurfaces on a log scale, spreading from the source to a small surface surrounding it. After a few milliseconds, the equipartition of the wavefield is reached for both metasurfaces, meaning that the elastic

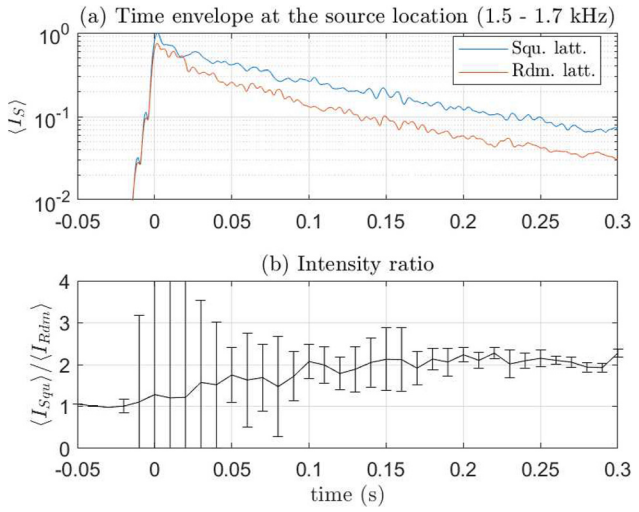

FIG. 5. (Color online) Intensity ratio in the frequency band from 1.5 Hz to 1.7 kHz between the random and regular square lattices. (a) Time envelope recorded at the source location. (b) Ratio between the square (regular) and random lattice intensities.

energy is equally spread in space and time. Figure 5(b) reports the ratio between the coherent intensity (measure in the regular square lattice) and the incoherent intensity (measured in the random lattice), with a factor of 2 retrieved, which is usually attributed to weak localization effects. Due to the equivalence of these two metasurfaces in terms of resonator density, materials, and surrounding plate geometry, the only remaining difference in this frequency regime is the constructive or destructive interference processes in the multiple scattering in each of the two metasurfaces. Indeed, a previous study on the same sample (Lott *et al.*, 2020) showed that the intrinsic attenuation coming from the beams and the plate does not play a major role in the apparent loss during the elastic wave propagation. In Fig. 5(b), each datapoint results from the spatial averaging that is needed to reach the required ensemble average. The error bars represent the spatial variabilities of the measures, which naturally decrease with time. The factor-2 ratio confirms the incoherent *versus* coherent scattering that occurs in the random *versus* regular, respectively, metasurfaces.

VI. LEAKAGE AT FLEXURAL RESONANCES AND NEGATIVE INDEX MATERIAL

In this last section, the effects of the flexural resonance are discussed in terms of the anisotropy and phase in the regular square lattice. The effects of the flexural resonances in the full A_0 bandgap have been discussed previously for the case of the random lattice (Rupin *et al.*, 2014, Lott and Roux, 2019b). Inside the passband, from the analysis of the apparent wave speed, there is no clear evidence of anisotropy at flexural resonances in the experimental data. However, inside the stopband, it is known that a negative refracting index can appear, which combines the monopolar and dipolar beam stress feedback at the plate surface (Colquitt *et al.*, 2016).

In the following, the first spatial analysis is reported for a regular lattice of the flexural leakage inside the main bandgap, and the emergence of the negative index material is discussed through the dispersion curve and the projection in the reciprocal space. The overall results are presented in Fig. 6. Here, in Fig. 6, panel 1, magnification of the dispersion curve for the regular square lattice from Fig. 2, panel 1, is shown, in the frequency band from 2.0 to 2.3 kHz. We highlight the three closed frequencies indicated as a–c in Fig. 6 (panel 2) for the (k_x, k_y) representation.

First, in contrast to the first main passband (Fig. 2, panel 2, <2 kHz), here (Fig. 6, panel 1) the experimental data deviate much more from the simulation in this frequency band. The wavenumber resolution of the experimental data is not sufficient to confirm without doubt the negative branch in the dispersion curve. However, this double negativity is confirmed experimentally in Fig. 6, panel 3, a–c, that shows a decrease in the radiation circle radius with frequency (i.e., from left to right). A rough estimation with azimuthal averaging of the radiation circles highlights a decrease in the wavenumber over a 60 Hz frequency bandwidth. We estimate around –3.3 m/s at 2150 Hz the group velocity, which is in the

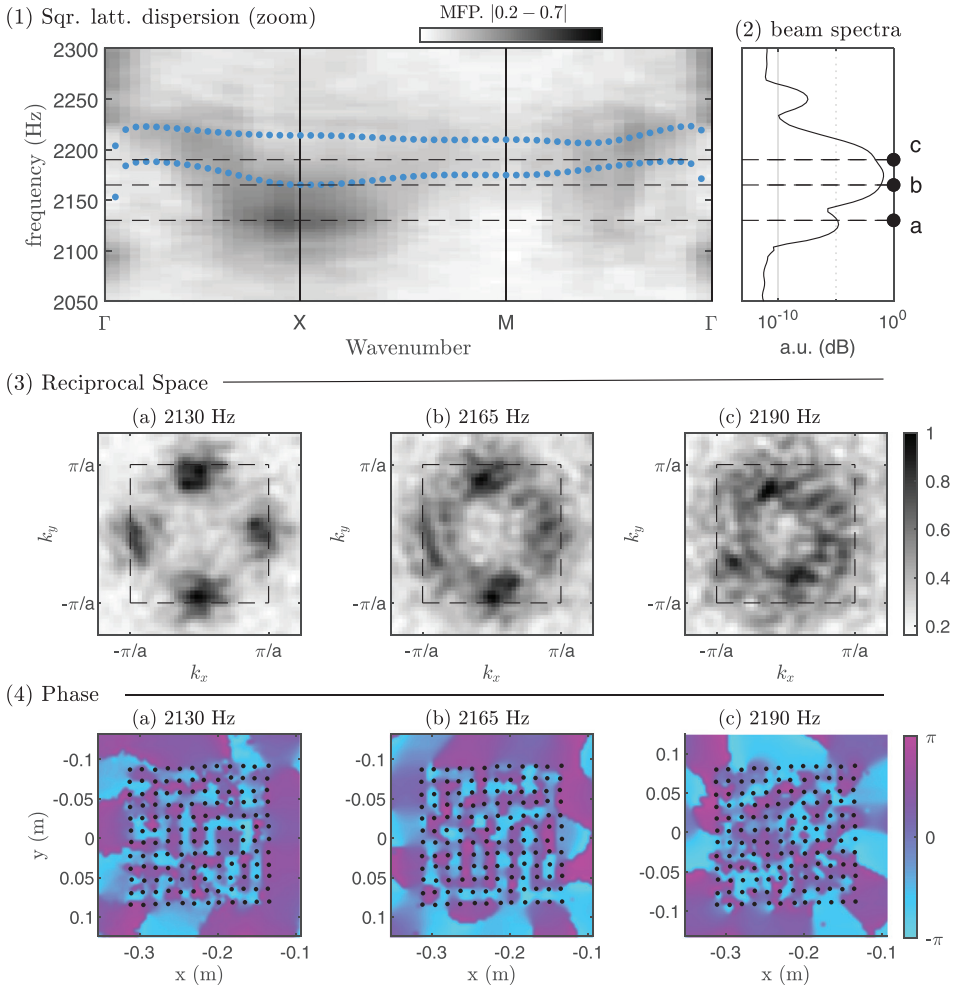

FIG. 6. (Color online) (1) Dispersion curves on the Brillouin edges between 2.05 and 2.3 kHz for the square (regular) lattice (as magnified from Fig. 2, panel 1). (2) Beam spectral motion (as magnified from Fig. 2, panel 3). (3) Reciprocal space imaging for the three frequencies a, b, and c from panel 1. (4) Phase representations of the wavefields for the same three frequencies as for a–c.

same order of magnitude (∼–2 m/s) as recently publish numerical simulation on a similar setup (Lott *et al.*, 2021). The fluctuations on the radiation circle in the measurement in Fig. 6, panel 3, a–c, suggests a large attenuation effect in the plate wave propagation. Recent numerical studies have shown that the transmission of energy through the flexural resonance motion is highly sensitive to small amounts of disorder in the beams positions (Lott *et al.*, 2021). We conclude that the loss is due to strong scattering effects coming from the imperfect position of the beams in our experimental realization of the square lattice metasurface, and not to intrinsic damping properties of the material.

Second, the phase representation of the wavefield in Fig. 6, panel 4, a–c, highlights particular behavior. The horizontal and vertical coherent lines seen in the phase pattern in Fig. 6, panel 4, a and b, suggest a collective motion of the aligned beams, with their vibration in phase. We interpret these coherent lines as synchronized dipoles associated with the flexural resonance of the beams (Lott *et al.*, 2020). The motion of the dipoles is aligned with the axis of symmetry (x–y) of the metasurface. As the frequency is increased from 2100 to 2200 Hz (Fig. 6, panel 3, a–c], the wavelength increases and the lines disappear. More surprising, as opposed to the results for the end of the passband (at 1750, 1830 Hz), the anisotropy highlights a different direction ($\Gamma - M$) of forbidden propagation in the flexural passband (2.0–2.2 kHz). Such behavior might be understood as a polarization effect of the resonance, with opposite mechanical conditions to be satisfied for a plane wave traveling in the diagonal direction of the unit cell ($\Gamma - M$). On the edges of the Brillouin zone, where there is a dipolar type of motion of the unit cell, the beam is located at a vibration node of the plate substrate, as illustrated in Fig. 6, panel 4, a. Consequently, in the ($\Gamma - M$) direction, a plane wave cannot at the same time verify in the perpendicular direction of propagation the two following conditions: (1) zero motion amplitude just below the beam–plate attachment; and (2) nonzeros motion amplitude at the unit-cell corner position. No out-of-plane motion can propagate in the ($\Gamma - M$) direction with a high k value, in contrast to the frequency of 1830 Hz, where the plate motion is maximal under the beams.

VII. CONCLUSIONS

In this paper, we report on an experimental comparison between two subwavelength metasurfaces made of two sets of closely positioned elongated aluminum beams (resonators) that are glued onto a thin aluminum plate with spatial organizations that provide random or regular structures. The consequences of these spatial arrangements are characterized through the dispersion curves, anisotropy, and

scattering properties for the two metasurfaces. We confirm a wideband Fano-like bandgap (monopolar scattering), a Bragg-induced bandgap, and a narrow bandgap (dipolar scattering), driven through the multimodal response of the resonators. In comparison to numerical simulations, the compressional resonance effects of the beams are correctly modeled with the Fano-like bandgap for the random and regular metasurfaces, and the Bragg bandgap for the regular lattice only. The flexural resonance effects, however, show less agreement between experiments and simulations, which we attribute to the building of the metamaterial. Finally, we illustrate a weak localization effect with an averaged measurement of the intensity at the source location, enlightening the different scattering regimes at play between two mesoscopic random and regular metasurfaces.

ACKNOWLEDGMENTS

The authors are grateful to Adrien Pelat, Mathieu Sécail, and Julien Nicolas from Le Mans Université, and to Pascal Audrain from IRT Jules Verne, for their strong contributions to the experiments using the so-called *3Dvib* platform located at the ENSIM School of Engineering in Le Mans.

Achaoui, Y., Khelif, A., Benchabane, S., Robert, L., and Laude, V. (**2011**). "Experimental observation of locally-resonant and Bragg band gaps for surface guided waves in a phononic crystal of pillars," Phys. Rev. B **83**(10), 104201.

Baggeroer, A. B., Kuperman, W. A., and Schmidt, H. (**1988**). "Matched field processing: Source localization in correlated noise as an optimum parameter estimation problem," J. Acoust. Soc. Am. **83**(2), 571–587.

Baravelli, E., and Ruzzene, M. (**2013**). "Internally resonating lattices for bandgap generation and low-frequency vibration control," J. Sound Vib. **332**(25), 6562–6579.

Cai, W., and Shalaev, V. M. (**2010**). *Optical Metamaterials*, Vol. 10 (Springer, New York).

Capolino, F. (**2017**). *Theory and Phenomena of Metamaterials* (CRC Press, Boca Raton, FL).

Colombi, A. (**2016**). "Resonant metalenses for flexural waves in plates," J. Acoust. Soc. Am. **140**(5), EL423–EL428.

Colombi, A., Craster, R. V., Colquitt, D., Achaoui, Y., Guenneau, S., Roux, P., and Rupin, M. (**2017**). "Elastic wave control beyond band-gaps: Shaping the flow of waves in plates and half-spaces with subwavelength resonant rods," Front. Mech. Eng. **3**, 10.

Colombi, A., Roux, P., and Rupin, M. (**2014**). "Sub-wavelength energy trapping of elastic waves in a metamaterial," J. Acoust. Soc. Am. **136**(2), EL192–EL198.

Colquitt, D. J., Colombi, A., Craster, R. V., Roux, P., and Guenneau, S. R. L. (**2017**). "Seismic metasurfaces: Sub-wavelength resonators and Rayleigh wave interaction," J. Mech. Phys. Solids **99**, 379–393.

Engheta, N., and Ziolkowski, R. W. (**2006**). *Metamaterials: Physics and Engineering Explorations* (John Wiley & Sons, New York).

Galich, P. I., Fang, N. X., Boyce, M. C., and Rudykh, S. (**2017**). "Elastic wave propagation in finitely deformed layered materials," J. Mech. Phys. Solids **98**, 390–410.

Juffmann, T., Ulbricht, H., and Arndt, M. (**2013**). "Experimental methods of molecular matter-wave optics," Rep. Prog. Phys. **76**(8), 086402.

Kaina, N., Fink, M., and Lerosey, G. (**2013**). "Composite media mixing Bragg and local resonances for highly attenuating and broad bandgaps," Sci. Rep. **3**, 3240.

Krushynska, A. O., Miniaci, M., Bosia, F., and Pugno, N. M. (**2017**). "Coupling local resonance with Bragg band gaps in single-phase mechanical metamaterials," Extreme Mech. Lett. **12**, 30–36.

Lauterbur, P. C. (**1973**). "Image formation by induced local interactions: Examples employing nuclear magnetic resonance," Nature **242**(5394), 190–191.

Lee, H., Lee, J. K., Seung, H. M., and Kim, Y. Y. (**2018**). "Mass-stiffness substructuring of an elastic metasurface for full transmission beam steering," J. Mech. Phys. Solids **112**, 577–593.

Leonhardt, U. (**2006**). "Optical conformal mapping," Science **312**(5781), 1777–1780.

Lott, M., and Roux, P. (**2019a**). "Effective impedance of a locally resonant metasurface," Phys. Rev. Mater. **3**(6), 065202.

Lott, M., and Roux, P. (**2019b**). "Locally resonant metamaterials for plate waves: The respective role of compressional versus flexural resonances of a dense forest of vertical rods," in *Fundamentals and Applications of Acoustic Metamaterials: From Seismic to Radio Frequency*, *Volume 1*, edited by V. Romero-Garcia and A.-C. Hladky-Hennion (John Wiley and Sons, Hoboken, NJ), pp. 25–45.

Lott, M., Roux, P., Rupin, M., Colquitt, D., and Colombi, A. (**2021**). "Negative index metamaterial through multi-wave interactions: Numerical proof of the concept of low-frequency Lamb-wave multiplexing," Sci. Rep. **11**(1), 1–8.

Lott, M., Roux, P., Seydoux, L., Tallon, B., Pelat, A., Skipetrov, S., and Colombi, A. (**2020**). "Localized modes on a metasurface through multi-wave interactions," Phys. Rev. Mater. **4**(6), 065203.

Matlack, K. H., Bauhofer, A., Krödel, S., Palermo, A., and Daraio, C. (**2016**). "Composite 3D-printed metastructures for low-frequency and broadband vibration absorption," Proc. Natl. Acad. Sci. **113**(30), 8386–8390.

Miniaci, M., Marzani, A., Testoni, N., and De Marchi, L. (**2015**). "Complete band gaps in a polyvinyl chloride (PVC) phononic plate with cross-like holes: Numerical design and experimental verification," Ultrasonics **56**, 251–259.

Miroshnichenko, A. E., Flach, S., and Kivshar, Y. S. (**2010**). "Fano resonances in nanoscale structures," Rev. Mod. Phys. **82**(3), 2257–2298.

Page, J. H. (**2016**). "Focusing of ultrasonic waves by negative refraction in phononic crystals," AIP Adv. **6**(12), 121606.

Pendry, J. B. (**2000**). "Negative refraction makes a perfect lens," Phys. Rev. Lett. **85**(18), 3966.

Pendry, J. B., Schurig, D., and Smith, D. R. (**2006**). "Controlling electromagnetic fields," Science **312**(5781), 1780–1782.

Pennec, Y., Djafari-Rouhani, B., Larabi, H., Vasseur, J. O., and Hladky-Hennion, A. C. (**2008**). "Low-frequency gaps in a phononic crystal constituted of cylindrical dots deposited on a thin homogeneous plate," Phys. Rev. B **78**(10), 104105.

Pomot, L., Payan, C., Remillieux, M., and Guenneau, S. (**2020**). "Acoustic cloaking: Geometric transform, homogenization and a genetic algorithm," Wave Motion **92**, 102413.

Rupin, M., Lemoult, F., Lerosey, G., and Roux, P. (**2014**). "Experimental demonstration of ordered and disordered multiresonant metamaterials for Lamb waves," Phys. Rev. Lett. **112**(23), 234301.

Seydoux, L., de Rosny, J., and Shapiro, N. M. (**2017**). "Pre-processing ambient noise cross-correlations with equalizing the covariance matrix eigenspectrum," Geophys. J. Int. **210**(3), 1432–1449.

Smith, D. R., Pendry, J. B., and Wiltshire, M. C. (**2004**). "Metamaterials and negative refractive index," Science **305**(5685), 788–792.

Tallarico, D., Movchan, N. V., Movchan, A. B., and Colquitt, D. J. (**2017**). "Tilted resonators in a triangular elastic lattice: Chirality, Bloch waves and negative refraction," J. Mech. Phys. Solids **103**, 236–256.

Veselago, V. G. (**1967**). "Electrodynamics of substances with simultaneously negative values of ε and μ," Usp. Fiz. Nauk. **92**, 517–526.

Williams, E. G., Roux, P., Rupin, M., and Kuperman, W. A. (**2015**). "Theory of multiresonant metamaterials for A_0 Lamb waves," Phys. Rev. B **91**(10), 104307.

Wu, Y., Lai, Y., and Zhang, Z. Q. (**2011**). "Elastic metamaterials with simultaneously negative effective shear modulus and mass density," Phys. Rev. Lett. **107**(10), 105506.

Yves, S., Berthelot, T., Fink, M., Lerosey, G., and Lemoult, F. (**2018**). "Measuring Dirac cones in a subwavelength metamaterial," Phys. Rev. Lett. **121**(26), 267601.

Yves, S., Berthelot, T., Lerosey, G., and Lemoult, F. (**2020**). "Locally polarized wave propagation through crystalline metamaterials," Phys. Rev. B **101**(3), 035127.